Effect of synthesis medium on aggregation tendencies of ZnO nanosheets and their superior photocatalytic performance

Richa Khokhra · Raj Kumar Singh ·
Rajesh Kumar

Abstract A simple soft chemical method has been suggested for large-scale production of zinc oxide (ZnO) nanosheets at room temperature using two synthesis mediums: aqueous (H_2O) and non-aqueous (C_2H_5OH). In H_2O medium, nanosheets interwoven group wise in *flower-like* structures revealing the strong inter-hydrogen bonding among initially nucleated ZnO nanocrystals, whereas weak hydrogen bonding in C_2H_5OH medium leads to the formation of un-aggregated interwoven' nanosheets. The growth of ZnO *flower-like* and *interwoven* nanosheets proceeded via anisotropic oriented attachment of ZnO nanocrystals. Obtained nanosheets were faceted, possessing large surface area, width hundreds of nanometers, and thickness in tens of nanometer, as characterized by scanning electron microscopy and transmission electron microscopy. These nanosheets show high sunlight photocatalytic activity toward the degradation of an organic pollutant 'methylene blue dye.' The enhancement in photodegradation efficiencies, *interwoven* sheets 99.94 %, and *flower-like* nanosheets 79.76 % for 120 min of irradiation is attributed to the surface oxygen vacancies narrowing the band gap as confirmed by photoluminescence spectra, faceted geometry, and large surface area of ZnO nanosheets.

R. Khokhra · R. Kumar (✉)
Jaypee University of Information Technology, Waknaghat,
Solan 173234, Himachal Pradesh, India
e-mail: rajeshkumarf11@gmail.com

R. K. Singh
Indian Institute of Petroleum, Dehradun 248005, India

Introduction

Zinc oxide (ZnO) nanostructures show many interesting physical and chemical properties such as optical, electronic, catalyst, photocatalysts, etc. [1–9]. In recent years, especially for industrial wastewater treatment for environmental remediation, the ZnO has attracted great attention [10] owing to its high quantum efficiency, excellent thermal and chemical stability, non-toxicity, low cost, and high photocatalytic efficiency for decomposing organic pollutants in water [11–13]. However, the wide bandgap 3.2 eV ($\lambda = 380$ nm) of ZnO restricts its use only in UV region, exhibiting hardly no response to the visible light as about 3–5 % spectrum of visible light falls in UV region limiting its photocatalytic efficiency. Several efforts have been made to overcome this disadvantage and to expand visible light absorption such as by doping with Co, Mn, Ni, N, etc. element, which narrows the band gap of ZnO, coupling of ZnO with other oxides like ZnO/SnO_2 and ZnO/ZnO_2, and deposition of Fe_2O_3, WO_3, and CdS on ZnO substrate [14]. In addition, concentration of oxygen vacancy defects on the surface [15–17], shape and size of nanostructures [18], existence of facets [19–21], and surface area [22, 23] are also discovered as important factors to enhance the photocatalytic activity of undoped ZnO.

The oxygen vacancy defects are kind of self-doping without addition of external impurities, which enhances the visible photocatalytic activity by narrowing the bandgap [24] while preserving the intrinsic crystal structure unlike to impurity doped ZnO. The oxygen vacancies induce visible spectrum absorption and enhance photocatalytic activity as reported by Li et al. for TiO_2 [24–26]. The surface oxygen vacancies act as the photoinduced charge trap and adsorption sites to diminish the probability of recombination of photoinduced electron–hole pairs [27]. The photocatalytic activity

is mainly a surface phenomenon; therefore, nanostructures perform much better than their bulk counterpart. Besides that, the photocatalytic activity is not only dependent on surface oxygen vacancies but also influences to the shape of nanostructures. As reported earlier, the polar surfaces of ZnO demonstrate greater photocatalytic activity than its non-polar surfaces [28, 29]. It is demonstrated that due to the surface positivity of (0001) polar surface, the OH$^-$ ion gets adsorbed preferably on it, which then reacts with hole (h$^+$) and generates reactive OH radical, thereby enhancing the photocatalytic activity. Compared with spherical nanocrystals, the one-dimensional (1D) nanostructures would have larger number of h$^+$ and e$^-$, determining the photocatalytic reaction rate, on the faceted surfaces/active sites, which results from the dimensional anisotropy [19, 20]. Conclusively, utilization of ZnO structures of large surface area, large number of oxygen vacancy defects, and faceted surfaces would enhance photocatalytic activity.

Nanostructures shape with large surface area depends upon the synthesis methods. Although there are several approaches to tune the shape and size of ZnO nanostructures, they are synthesized by hydrolytic method explained elsewhere [30]. In hydrolytic method, the controlled ZnO nanostructures are obtained using templates [21, 31–38], or properly selecting (structure directing) a hydrolyzing agent [39, 40] or reaction media [41, 42]. A template provides the shape/size to the nanostructures by confining the reaction in a restricted space [36]. Similarly, a hydrolyzing agents act as a soft template, which controls the shape/size of nanostructures e.g., the room temperature ionic liquids (RTIL) form different pre-organized solvent structures, which assist in the anisotropic growth of nanostructures [38, 43]. In case of reaction media, the reaction media controls the rate of hydrolysis thereby controlling the growth process and, hence, the shape/size of nanostructures [39, 44]. Now, so far the increase in the number of oxygen vacancies is concern, it is basically related with the disorders at higher temperature. Although converting white color of ZnO nanostructures to yellow is an enhancement in oxygen vacancies, however, in most of ZnO nanostructures except perfect single crystals [45], the oxygen vacancy defects always exist. There are various studies on the surface oxygen vacancies of the ZnO nanosheets [46–51] but it is rarely reported the formation of ZnO nanosheets without surfactant, directing agent and templates.

The ZnO nanostructure with large surface area, which remains stable against aggregation and possess faceted surface to enhance photocatalytic activity, still remains a challenge. Herein, for the first time, we demonstrate different aggregation tendencies of ZnO nanoparticles, which lead to the formation of faceted ZnO un-aggregated interwoven nanosheets and group wise interwoven i.e., flower-like nanosheets in different reaction mediums without utilizing

template or directing agent at room temperature. Although similar ZnO structures have been already synthesized in many cases using templates, directing agents and surfactants [46, 52–54], in this work, we have prepared ZnO nanosheets without surfactant, directing agent and templates. In whole of the discussion, we would call un-aggregated interwoven nanosheets simply as 'interwoven' nanosheets and group-wise interwoven i.e., flower-like nanosheets as 'flower-like' nanosheets. In this work, the alcoholic (C$_2$H$_5$OH) medium leads to the formation of ZnO *interwoven* nanosheets, whereas *flower-like* nanosheets were obtained in aqueous medium. The obtained faceted ZnO *interwoven* nanosheets and *flower-like* nanosheets having large surface area were used for sunlight photocatalytic purification of organic pollutant 'methylene blue (MB) dye' from water. The obtained significantly high photocatalytic activity is due to the oxygen vacancies, large surface area, and faceted structure of the as-synthesized ZnO nanosheets.

Experimental

Zinc acetate dihydrate (Zn(CH$_3$COO)$_2$·2H$_2$O) was purchased from Sigma-Aldrich (USA), and potassium hydroxide (KOH) was purchased from Merck (India). All the reagents used in this experiment were analytically pure and used without further purification. In a typical synthesis process, ZnO nanosheets were synthesized separately in alcoholic (C$_2$H$_5$OH) and aqueous (deionized H$_2$O) medium, respectively. Two 0.5 mol/L solutions of zinc acetate dihydrate (Zn(CH$_3$COO)$_2$·2H$_2$O) were formed separately in C$_2$H$_5$OH and H$_2$O. A 25 mL solution of KOH was then added dropwise in each of the solutions under vigorous stirring condition at room temperature. To monitor growth mechanism (i.e., pattern) of ZnO nanostructures, samples were collected at 0.25, 1, 2, and 4 h of time intervals from the reaction mixture. Collected precipitate was filtered and washed with deionized water and ethanol to remove undesirable ions such as CH$_3$COO$^-$, and K$^+$ was dried at 100 °C for 1 h, which yielded to a ZnO powder in both synthesis medium cases. The obtained nanopowders were examined by field emission scanning electron microscopy (FESEM) for morphological investigation, X-ray Diffractometer (XRD) and high-resolution transmission electron microscopy (HRTEM) for crystallographic information, Fourier transform infra red (FTIR) spectroscopy for functional group analysis, and photoluminescence (PL) for surface oxygen vacancy defects and Brunauer–Emmett–Teller (BET) surface area measurement.

The photocatalytic activities were investigated for both of ZnO nanosheets and synthesized for 4 h reaction time in C$_2$H$_5$OH and H$_2$O mediums, respectively. The MB dye was used as degraded material in quartz beakers. A 50 mg of

Fig. 1 FESEM images of ZnO nanosheets synthesized at room temperature in ionic mediums for 4 h of reaction time. **a**, **b** are *interwoven* nanosheets at different magnifications synthesized in H_2O medium, and **c** is corresponding XRD pattern. **d**, **e** show *flower-like* nanosheets synthesized in C_2H_5OH medium, and **f** is corresponding XRD pattern
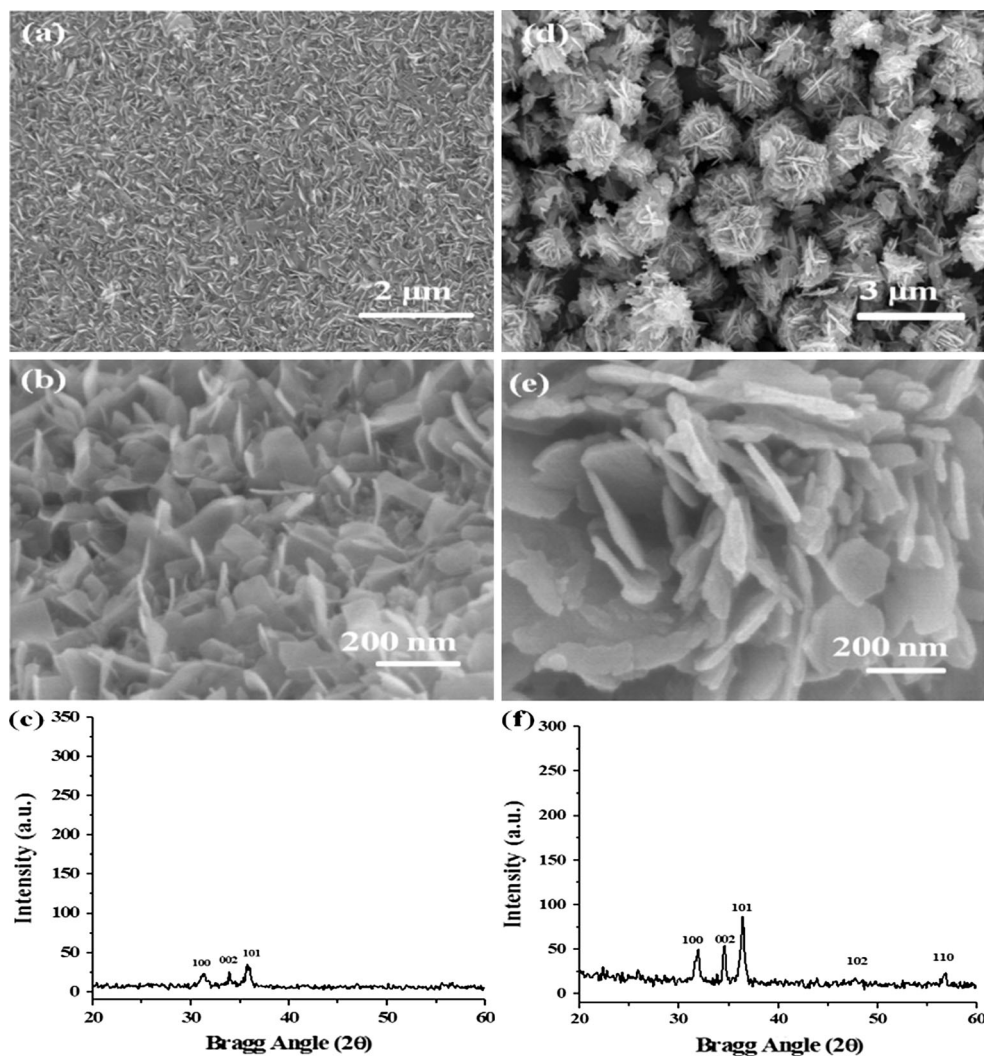
each ZnO nanosheets was dispersed separately in 150 mL aqueous solutions of MB formed with initial concentration 20 mg/L. The mixtures after sonicating for 15 min and stirred for 15 min were exposed to sunlight. The experiment was performed from 9:00 am to 2:00 pm on a sunny day (6 % clouds and 34 % humidity) on April 29 and April 30, 2014 in Solan city, India (geographical location: 31.15 degree north latitudes and 77.20 degree east longitude, environmental temperature: 25 °C). The small aliquots (5 mL) were drawn from the reaction mixture at fixed interval, subsequently centrifuged at a rate of 5000 rpm for 10 min, and monitored for the absorbance at a wavelength of 660 nm. The degradation of MB was monitored using the UV–Vis spectrophotometer.

Results and discussion

The product synthesized in C_2H_5OH media for prolonged '4 h' of reaction time was characterized by FESEM, as

shown in Fig. 1a, b. Figure 1a is low-magnification image showing large-scale synthesis of the product, and Fig. 1b shows higher magnification FESEM image showing *interwoven* nanosheet structure. The obtained nanosheets are of width about 200 nm and thickness in tens of nanometers, and are interwoven to each other as in Fig. 1b. The crystal structure of these *interwoven* nanosheets investigated by X-ray diffraction (XRD) is shown in Fig. 1c. Diffraction peaks at $2\theta = 32.7°$, $34.5°$, and $36.42°$ in XRD pattern could be assigned the (100), (002), and (101) lattice planes of ZnO (JCPDS file no. 36–1451). The well-matched diffraction peaks and calculated lattice constants $a = 3.253$ Å and $c = 5.211$ Å indicate hexagonal crystal structure of obtained ZnO nanosheets.

Similarly, the product synthesized in H_2O media for 4 h of reaction time was characterized by FESEM that is shown in Fig. 1d, e. Figure 1d shows large-scale synthesis of the product, and from Fig. 1e it can be observed that the nanosheets are interwoven groupwise in the *flower-like* structure, so we can call them as *flower-like* nanosheets.
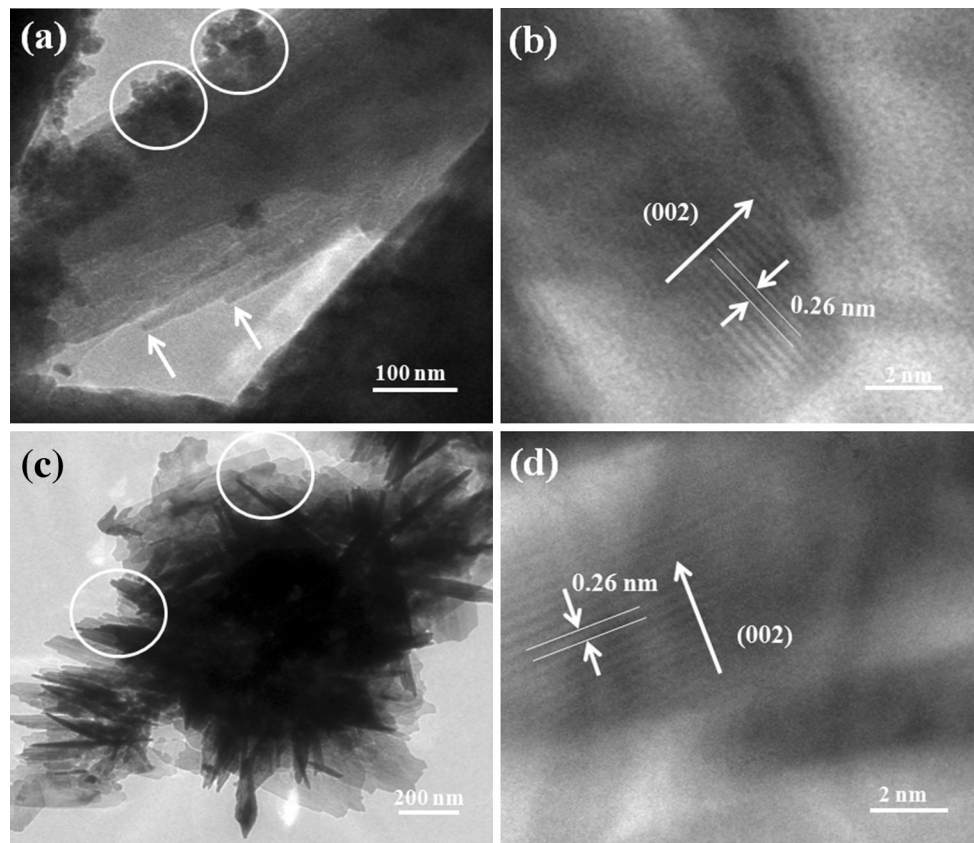
Fig. 2 TEM images of ZnO *interwoven* and *flower-like* nanosheets **a** show the *interwoven* nanosheets with facet edges indicated by *arrows*, and nanoparticles on the surface of nanosheet enclosed by *circles*, **b** high-resolution TEM image, **c** the *flower-like* nanosheets with facet edges as *encircled*, and **d** high-resolution TEM image of *flower-like* nanosheet

The *flower-like* nanosheet structure was resulted due to higher extent of aggregation of initially nucleated ZnO nanocrystals unlike to the case of *interwoven* nanosheets. The size of flower structure is about 2 μm indicating nanosheet width as 2 μm, also the thickness of nanosheets in these *flower-like* structures is about 25 nm as in case of *interwoven* nanosheets. In XRD pattern as shown in Fig. 1f, diffraction peaks at $2\theta = 32.7°$, 34.5°, and 36.42° could be assigned as the (100), (002), and (101) lattice planes of ZnO similar to the case of *interwoven* nanosheets except that in this case obtained peaks are intense as compared with *interwoven* nanosheets. The observed lattice constants (a = 3.256 Å and c = 5.211 Å) indicate the formation of hexagonal phase structure similar to the *interwoven* nanosheets. The obtained higher intensity of peaks can be expected due to denser geometry of *flower-like* nanosheets, which might result in large counts in XRD. Both *interwoven* nanosheets and *flower-like* nanosheets show some weak orientations as well in XRD pattern at $2\theta = 47.44°$ and 56.58°, which corresponds to lattice planes (102) and (110).

To investigate crystal structure and growth direction of nanosheets, we analyzed *interwoven* and *flower-like*

nanosheets by TEM. Figure 2a shows TEM image of *interwoven* nanosheet. The nanosheet has faceted edges as indicated by arrows in Fig. 2a. In this image, some nanocrystals (encircled) are also observed attached on the surface of nanosheet. The presence of faceted edges and nanocrystals in TEM image indicates that the growth of nanosheet would have proceeded via oriented attachment [55–57] of nanocrystals at the faceted edges. The nanocrystals formed in solution would have attached orientedly to create a new faceted surface, and the process of oriented attachment continues until the precursor inside the solution is consumed completely. In HRTEM image of *interwoven* nanosheet, the lattice spacing 0.26 nm as shown in Fig. 2b corresponds to the growth direction (002) of wurtzite structure of ZnO. Similarly, the TEM image (Fig. 2c) of *flower-like* nanosheets also shows faceted edges indicating the growth process via oriented attachment of nanocrystals. Also, the similar lattice spacing 0.26 nm (Fig. 2d) as that of *interwoven* nanosheets corresponds to the growth direction (002) of wurtzite structure of ZnO. Therefore, both the ZnO nanostructures *interwoven* nanosheets and *flower-like* nanosheets have faceted edges and are grown via oriented attachment of nanocrystals along 002
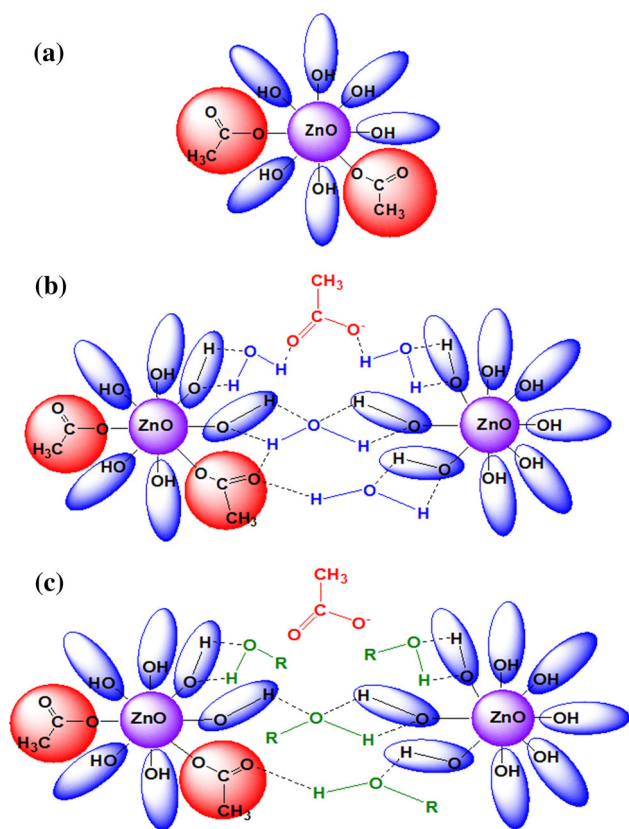
Fig. 3 Aggregation mechanism of ZnO nanocrystal **a** hydroxyl and acetate ion adsorbed on ZnO, **b** strong hydrogen bonding network in water solvent, and **c** weak hydrogen bonding network in alcohol solvent condition

directions. The TEM observations show that both *inter-woven* and *flower-like* nanosheets are faceted, and for both ZnO nanosheets, the XRD and TEM parameters are similar except that *flower-like* nanosheets result from higher aggregation tendency of ZnO nuclei in aqueous medium.

Investigation of different aggregation tendencies of ZnO nanocrystals in H_2O and C_2H_5OH mediums

We tried to investigate the reason behind the different aggregation tendencies of initially nucleated ZnO nanocrystals in H_2O and C_2H_5OH medium, which leads to the formation of *interwoven* nanosheets and *flower-like* nanosheets with the reaction time. We presumed that difference in the aggregation tendencies is attributed to the extent of hydrogen bonding. After formation of ZnO nanocrystals, the residual OH^- and CH_3COO^- ions remain adsorbed on the surface of ZnO nuclei as shown by schematic in Fig. 3a. The CH_3COO^- ions adsorbed on ZnO nuclei help not only in hydrogen bonding but also in stabilizing such bonding (Fig. 3c) in free form in crystal. A strong hydrogen bonding network exists between the adjacent ZnO

nuclei (Fig. 3b) in case of H_2O medium due to extremely high polarity of water.

However, in C_2H_5OH medium, such a hydrogen bonding is relatively weak due to interference of bulky ethyl groups and lower polarity of ethanol. Therefore, the aqueous medium is more favorable for the aggregation of nanocrystals than alcoholic medium. To confirm the assumption, the ZnO nanostructure samples were investigated by FTIR. The FTIR spectra contain broad peaks in both the cases (Fig. 4a, b) at around 3392 and 1635 cm^{-1}, which are assigned to the stretching and bending modes, respectively, of hydroxyl groups (chemisorbed and/or physisorbed H_2O molecules) on the surface of ZnO nanocrystals. A band at 1403 cm^{-1} related to the symmetrical/asymmetrical stretching modes of the carboxylate group of acetate coordinated to the surface of ZnO nanocrystals can be observed. Also, a high-intensity broad band around 884 cm^{-1} due to the typical bending mode of hydroxyl group is observed in the spectra of these structures as shown in Fig. 4a, b. Other unsigned peaks are attributed to remnant organic species in the samples. The observed growth direction (002) in TEM characterization for both the ZnO nanostructures i.e., *flower-like* and *interwoven* nanosheets indicates that the mediums affect only aggregation tendencies of initially formed nanocrystals and not the direction of growth of nanosheets.

In view of the possibility of occurrence of symmetry distortion in the –OH stretching band due to existence of hydrogen bonding, this distortion (i.e. $\Delta_{1/2}$) among corresponding peaks was compared using a reported method [58] and calculated. The difference in the –OH stretching peak symmetry (between 2750 and 3750 cm^{-1}) can be clearly seen in the spectra Fig. 4c, d. First, a vertical line starting from the bottom of the peak was constructed parallel to y-axis. Similar straight lines were also drawn parallel to x-axis at various percent transmittances (%T). Then on each line, the distance from the vertical one to the right and left was measured. By taking the difference between two measurements (½ left–½ right), $\Delta_{1/2}$ was calculated as

$$\Delta_{1/2} = (\partial a + \partial b + \partial c + \partial d)/4,$$

where $\partial a = a_1 \sim a_2$, $\partial b = b_1 \sim b_2$, $\partial c = c_1 \sim c_2$, $\partial d = d_1 \sim d_2$.

Although the difference is very small, the symmetry distortion is found to be higher in case of nanocrystals from H_2O medium revealing the strong inter-hydrogen bonding among these ZnO nanocrystals as compared to the ZnO nanocrystals obtained from C_2H_5OH medium (Fig. 4c, d). The possible distortion of –OH band can be influenced by many factors among others amount of OAc anions on the surface or different morphology. But in present work, –OH band distortion due to the OAc anions amount on the surface could be ruled out as the ZnAc$_2$ concentration is
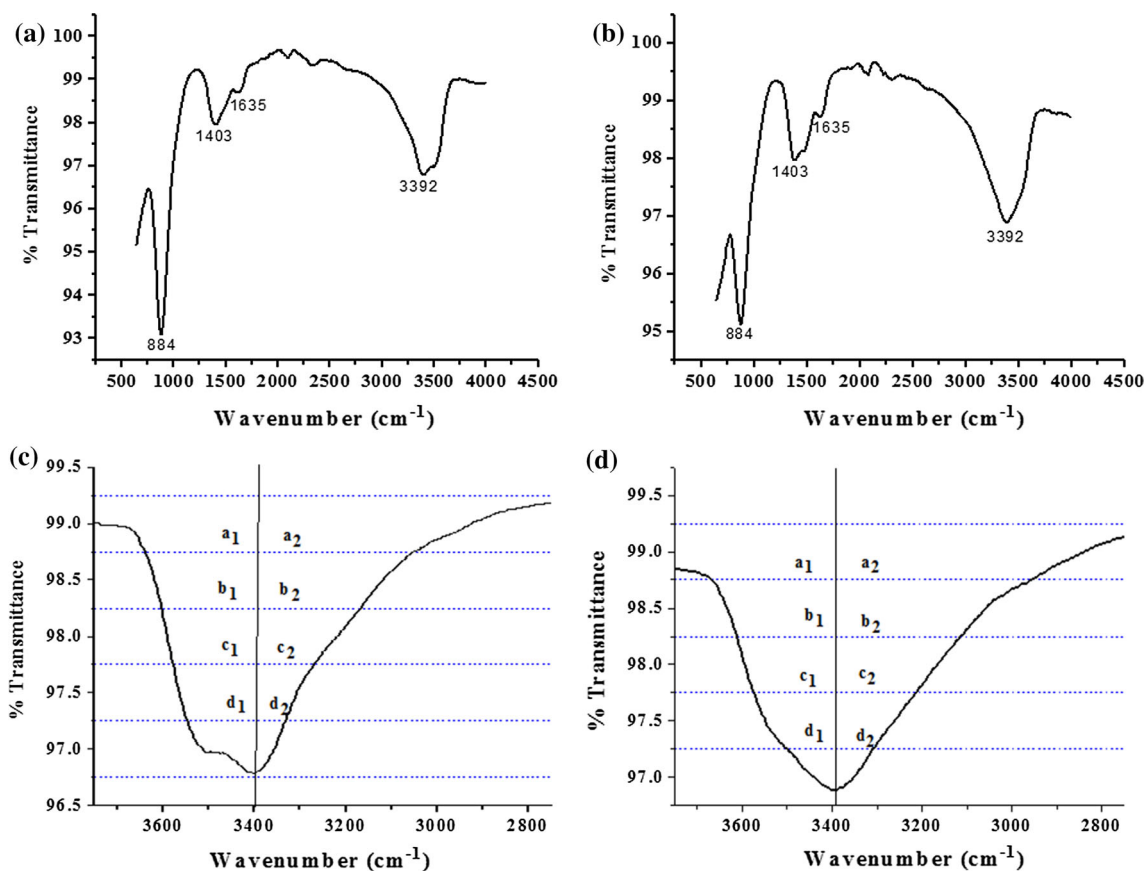
Fig. 4 FTIR spectra of a *interwoven* nanosheets and b *flower-like* nanosheets show IR absorption frequencies of organic functional groups and their respective spectra c and d for determining symmetry distortion between 2750 and 3750 cm^{-1}

same in both the medium. As far as the different morphology is concerned, there is no report having evidence of IR band symmetry dependence on the morphology so far. Stretching peak symmetry distortion is an exclusive phenomenon of hydrogen bonding.

Confirming different aggregation tendencies of ZnO nuclei in the respective mediums, the mechanism of nanosheets growth is an interesting step to discuss. To propose a formation mechanism of ZnO *interwoven* nanosheets and *flower-like* nanosheets, we monitored the product at different time intervals i.e., 0.25, 1, 2, and 4 h. All the collected samples were filtered, washed with deionized water, dried at 100 °C for 1 h, and subjected to FESEM investigation. Figure 5 shows FESEM image of ZnO nanostructures synthesized in C_2H_5OH and H_2O mediums at successive stages of reaction. In the beginning when the reaction proceeded for 0.25 h, nanocrystals of size about 25 nm were formed as shown in Fig. 5a–c, however, with different aggregation tendencies. The nanocrystals formed in H_2O medium are more aggregated as compared with that formed in C_2H_5OH medium. The different aggregation tendencies of nanocrystals in C_2H_5OH and H_2O mediums appear clearly in successive stages of the growth as shown in Fig. 5. Figure 5d shows

that scattered nanosheet-like structures with some nanoparticles start to appear for 1 h of reaction time in C_2H_5OH medium, whereas in case of H_2O medium for same reaction time, aggregated nanosheets along with few nanocrystals are formed as shown in Fig. 5e, f. For 2 h of reaction time, the nanosheets formed in C_2H_5OH medium are interwoven as shown in Fig. 5g, and the aggregated nanosheets formed in H_2O medium appears in *flower-like* structure as shown in Fig. 5h, i. In Fig. 5i, clear faceted edges of nanosheets along with some attached nanocrystals can be seen, suggesting the oriented attachment process of growth. When the reaction was preceded for 4 h of reaction time, in SEM (Fig. 5j–l) images of ZnO nanostructures, no nanocrystal is observed, which again indicates that the nanosheets grow at the expanse of the nanocrystals.

In nut shell, the whole process of formation of ZnO nanostructures i.e., *interwoven* nanosheets and *flower-like* nanosheets may be described to proceed via the nucleation of ZnO nanocrystals, their different aggregation in respective mediums and then subsequent directional growth to form nanosheet structures. The nucleation takes place in a condition when the concentration of precursors (i.e., nanocrystals or monomers) exceeds the critical super saturation level. In such a condition, smaller nanocrystals

Nanosheets (in C₂H₅OH medium)

Nanosheet flowers (in H₂O medium)
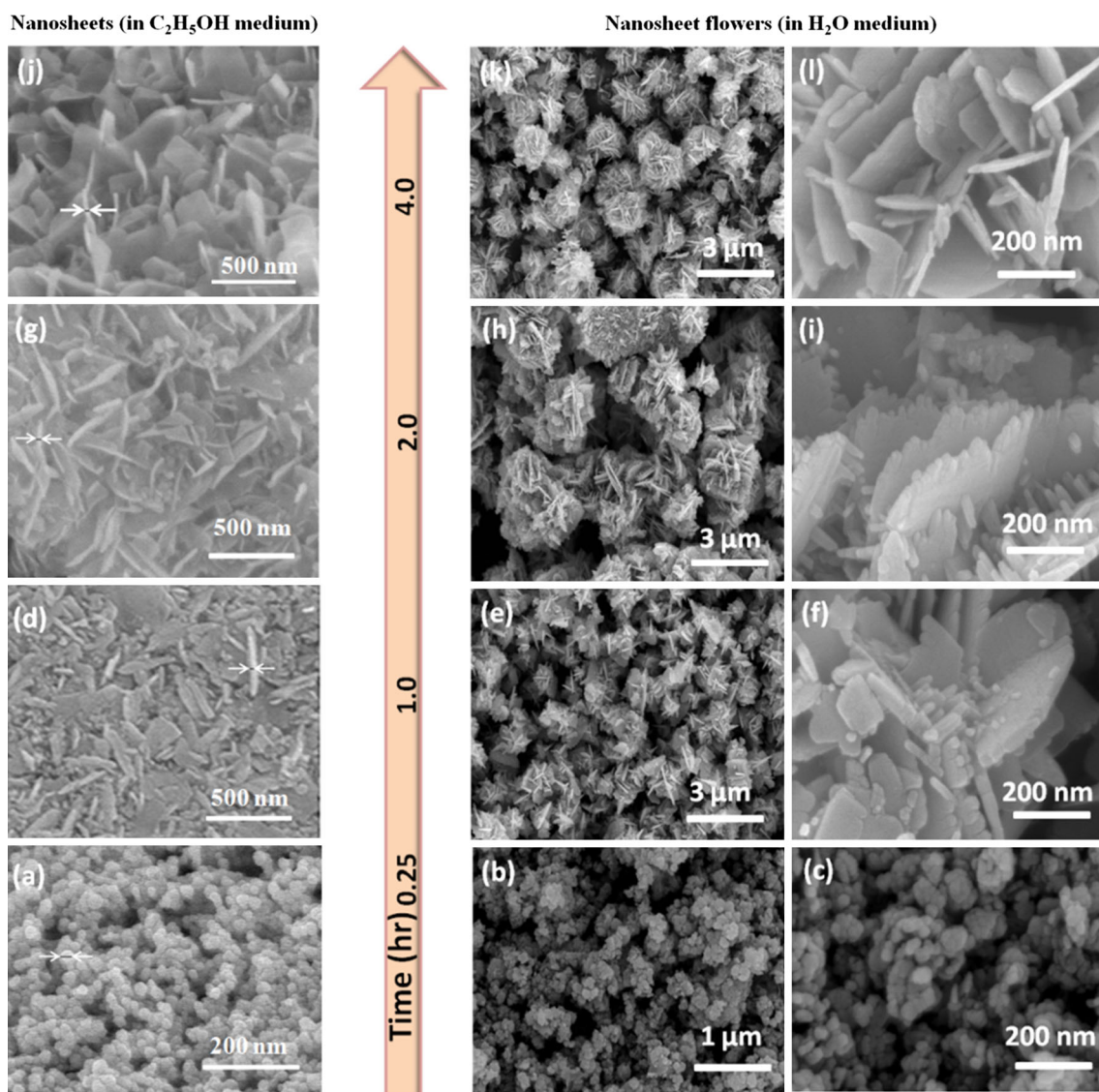
Fig. 5 Evolution of the ZnO nanostructures with the increase of reaction times: **a–c** are for 0.25 h, **d–f** are for 1 h, **g–i** are for 2 h, and **j–l** are for 4 h reaction time

grow rapidly until their concentration falls below the critical level for nucleation [59]. To understand the nucleation process, the chemical reaction must be understood. Initially, the Zn^{2+} from $ZnAc_2$ and OH^- ions from the medium (H_2O or C_2H_5OH) coordinate with each other to form an aggregate of the type $[Zn_x(OH)_y]^{(2x-y)+}$ [60], which after dehydration forms a small ZnO nanocrystal. These nanocrystals that are oriented randomly in the beginning start aggregating with different tendencies depending upon the medium (H_2O or C_2H_5OH). Such a tendency of initially formed ZnO nanocrystals is higher in aqueous medium than that in alcoholic medium (Fig. 5b). After aggregation of nanocrystals, the anisotropic growth, leading to the formation of *interwoven* nanosheets and *flower-like* nanosheets, may occur either by (i) collision (due to random Brownian motion) [61] and fusion between the particles,

known as *oriented attachment* [62] of nanocrystals or by (ii) exchange (dissolution and diffusion) of molecules between various particles, known as *Ostwald ripening* [63].

Since a hexagonal ZnO nanocrystal has two polar planes (±002) and six non-polar planes [64], the polar planes having relatively higher surface energy can promote the anisotropic growth in the ±001 directions. The polar ZnO nanocrystals show oriented attachment to minimize the overall system energy by rotating/piling up and then fusing with the attached nanocrystals [65]. Therefore, in the oriented attachment process, initially the randomly oriented ZnO nanocrystals aggregate, as indicated by encircles in Fig. 2a, and then with the passage of reaction time they might have rotated to ensure their orientations parallel to (±002) direction as indicated by arrows in Fig. 2a. Further, as the observed nanosheets are smooth (Fig. 5j–l), the

bottle neck between the adjacent nanocrystals may later when the precursor concentration is lowered, have filled up by the Ostwald ripening process and thus smoothening the surface of nanosheets [33]. In the other consideration, the anisotropic nanostructures may be supposed to be grown via directional Ostwald ripening process. In this process, similar to the above mechanism, initially, the randomly oriented ZnO nanocrystals aggregate, and then with the passage of reaction time smaller, nanocrystals dissolve into the solution and attach on the polar surfaces of larger nanocrystals in the aggregate, leading to the formation of oriented nanosheets in the aggregate. We know that when the precursor concentration falls below the nucleation concentration the nucleation stops. According to Ostwald ripening process [66, 67], the large nanocrystals grow at the cost of smaller nanocrystals. The growth of large nanocrystals proceeds by the capturing of Zn^+ ion formed from the dissolution of smaller nanocrystals and brought near to the surface of larger nanocrystals by the process of diffusion. These surface Zn^+ ions are terminated by OH^- ions available inside the solution. Thus, the growth continues further by capturing Zn^+ ions, OH^- ions followed by dehydration [59]. Owing to the higher surface energy of polar surfaces of ZnO nanocrystals, the ions Zn^+ and OH^- adsorb favorably on the polar surfaces. Such a process is repeated over the time leading to the directional (±002) growth of nanosheets. Although both of the growth mechanisms can be suggested for the obtained ZnO nanostructures, from TEM observations, the oriented attachment of nanocrystals followed by Ostwald ripening process smoothening the surface is more plausible.

Photocatalytic performance of ZnO interwoven nanosheets and flower-like nanosheets: organic pollutant removal

The photocatalytic activity of *interwoven* and *flower-like* nanosheets as catalyst for the degradation of MB was investigated under sunlight irradiation. The degradation of MB by both of the ZnO nanostructures was carried out in the similar conditions. For this purpose, 0.34 g/L of ZnO nanosheets was added into 6.25×10^{-5} M of MB solutions. The change in optical absorption spectra with the degradation of MB dye by *interwoven* and *flower-like* nanosheets for different time intervals under sunlight irradiation is shown in Fig. 6. The observed decrease in the absorption band intensities of MB indicates that MB gets degraded by both ZnO nanostructures. In case of *interwoven* nanosheets, the disappearance of the characteristic band of MB dye at 660 nm after 2 h of sunlight irradiation (Fig. 6a) indicates that MB has been degraded completely by *interwoven* nanosheets. For the similar conditions in case of *flower-like* nanosheets, there exists the characteristic peak of the MB dyes solution indicating the presence of MB molecules in the solution as shown in Fig. 6b. The progress of photodegradation of MB dye by both ZnO nanostructures under sunlight irradiation can simply be realized by the color change of solution as shown in the inset of Fig. 6.

Figure 7 shows the relative concentration C/C_0 of MB dye with irradiation time, where C_0 is MB dye's initial concentration after the equilibrium adsorption of ZnO nanosheets and C is concentration of MB at time t. Figure 7 shows that under sunlight irradiation, the self-degradation of MB without introducing ZnO nanosheets is negligible, whereas its concentration decreases rapidly in the presence of ZnO nanosheets. The photocatalytic efficiency was calculated using the expression $\eta = (1 - C/C_0) \times 100$, where C_0 is the concentration of MB before illumination and C is the concentration after irradiation time. Figure 7 shows the photocatalytic efficiency, and the MB dye is removed around 100 % while using *interwoven* nanosheets, whereas the *flower-like* nanosheets remove around 80 % when irradiated for 120 min in sunlight.

Figure 8 shows the plots between $\ln(C_0/C)$ and irradiation time. A linear relationship between $\ln(C_0/C)$ and

Fig. 6 Time-dependant absorption spectra of MB dye solution under sunlight irradiation with catalyst **a** ZnO *interwoven* nanosheets and **b** ZnO *flower-like* nanosheets
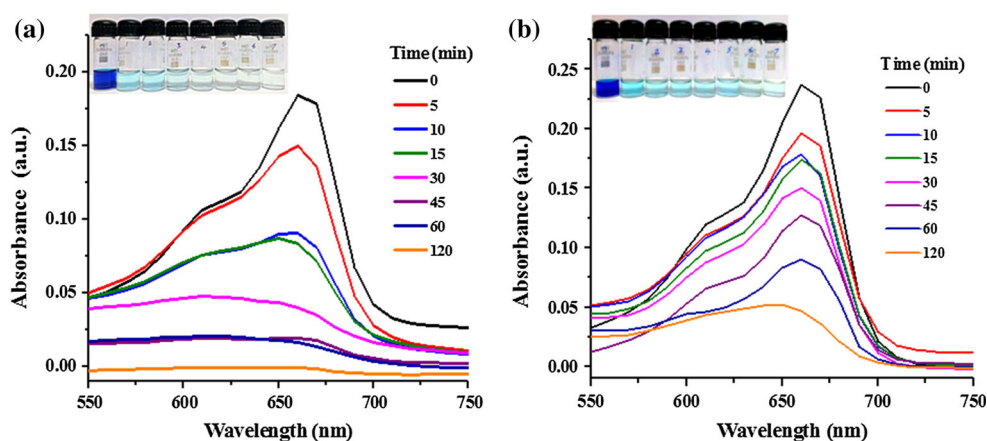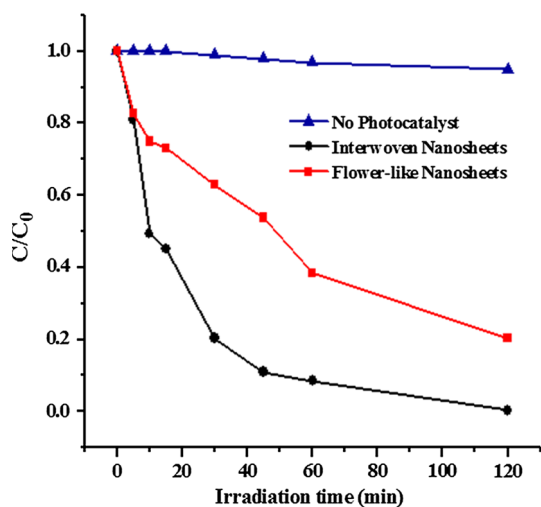
Fig. 7 *Plot* represents photocatalytic activity of *interwoven* nanosheets and *flower-like* nanosheets as catalysts under sunlight irradiation
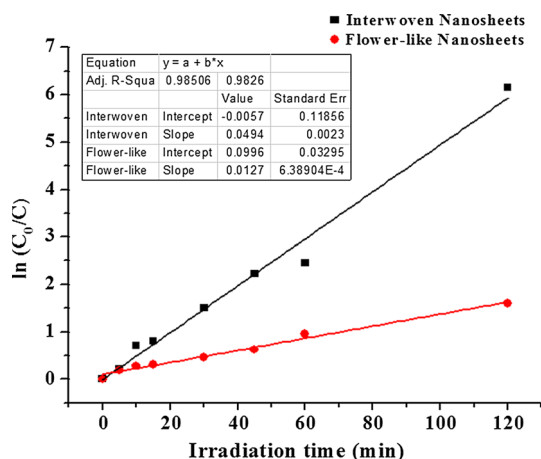
Fig. 8 *Plots* for photocatalytic kinetics analysis for the degradation of MB with both type of ZnO nanosheets (initial concentration of MB = 10^{-5} M)

irradiation time indicates that the photodegradation of MB dye, by *interwoven* and *flower-like* ZnO nanostructures, proceeds via a pseudo-first-order kinetic reaction i.e., $\ln(C_0/C) = kt$, where k is the photodegradation rate constant. The corresponding parameters of degradation and pseudo-first-order model for ZnO nanostructures are summarized in Table 1.

We also investigated the degradation in photocatalytic performance of ZnO nanosheets. For this reason, ZnO *interwoven* and *flower-like* nanosheets were used for three photocatalytic cycles. In each cyclic run, the photocatalytic experiment was performed as mentioned earlier using the concentration 0.34 g/L of ZnO nanostructures and

6.25×10^{-5} M of MB dye. The degradation of MB dye was investigated by UV–Vis spectrophotometer. After each run, the ZnO nanosheets were separated from the solution by centrifugation, which was reused after drying at 100 °C. Figure 9 shows the degradation of MB dye under sunlight irradiation for three cycles. From Fig. 9, it is observed that after three catalytic cycles, there appeared a very negligible degradation in the photocatalytic performance of both types of ZnO nanosheets.

Photocatalytic mechanism

Since photocatalytic activity is a surface phenomenon, therefore, a nanoscale ZnO material is believed to perform much better than its bulk counterpart [68]. The basic mechanism of photocatalysis of ZnO is well established [55, 69–71]. Initially, when the solution was kept in dark for 30 min, the adsorption–desorption of MB on the surface of ZnO nanosheets occurred. As a photocatalytic phenomenon, when the solution was irradiated with sunlight, electron–hole pairs would have generated in ZnO nanosheets. However, as the band gap of ZnO is 3.3 eV, only UV light can excite the ZnO nanosheets to generate electron–hole pairs. The created holes initiate reaction either with electron-rich surface hydroxyl groups or adsorb water molecules to yield hydroxyl OH^-. On the other hand, the electrons react with the dissolved oxygen molecules to produce superoxide radical anions O_2^-. Thereafter, the superoxide radical anions O_2^- could yield hydroperoxyl radicals HO_2 and OH by the subsequent hydration processes. These resultant radicals (OH and O_2^-) are responsible for decomposition or mineralization of MB [72]. But as there is only 3–5 % of UV photons present in the sunlight, it should show poor photocatalytic efficiency [73]; therefore, we might consider other factors such as self-photosensitization of MB, ZnO surface oxygen vacancies, and the presence of facets on ZnO nanosheets, which enhance photocatalytic activity of ZnO.

The MB itself helps in enhancing the photocatalytic activity because it acts as a self-photosensitizer under sunlight irradiation [74]. It absorbs visible light and transfers the absorbed energy to other molecules [75–77]. The transfer of energy may occur via two different processes: electrons transfer process, forming exciplex; and the energy transfer process, exciting the molecule to higher energy state. In the energy transfer process, when MB is exposed to both oxygen (O_2) and sunlight, the excited state MB transfers energy to ground state O_2 (triplet) and converts it into the excited state O_2 (singlet) for photo-oxygenation [76]. The transfer process of electron from the dye to semiconductor, especially for ZnO, has also been reported previously as well [73]. But in our case, in the absence of photocatalyst (Fig. 7a), a negligible amount of

Table 1 ZnO as photocatalysts follow the pseudo-first-order kinetics (initial concentration of MB was 10^{-5} M)

Nanostructure	% Degradation (in 120 min)	k (min^{-1})	Correlation coefficient (R^2)	SE
Interwoven nanosheets	99.94	0.0494	0.98506	0.0023
Flower-like nanosheets	79.76	0.0127	0.98266	6.38904e−4
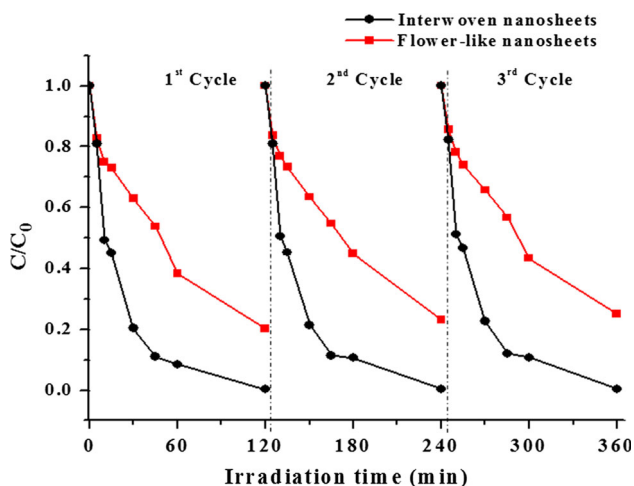
Fig. 9 Effect of number of runs on the degradation of MB dye in the presence of ZnO nanosheets as catalyst under sunlight irradiation (catalyst concentration: 0.34 g/L; initial concentration of dye: 6.25×10^{-5} M)

MB was degraded through 120 min of irradiation under sunlight. It indicates that the self-photosensitization process of MB can be neglected in our case.

Besides UV photon excitation of ZnO and self-sensitization of MB, the oxygen vacancies on the surface of ZnO nanostructures play very important role for enhancing the photocatalytic activity of ZnO. The oxygen vacancies not only form the active centers or trap centers for photoinduced charge [17, 78, 79] but also they narrow the band gap of ZnO. The narrowing of the energy band gap is induced by the surface oxygen vacancies by the broadening of valance band, which results for the generation of visible-light photoactivity in ZnO and, hence, the increase of the photocatalytic activity under sunlight irradiation. In our case, surface oxygen vacancies are considered as one of the factor enhancing the photocatalytic activities of both *interwoven* and *flower-like* nanosheets. We used PL measurements to confirm the existence and properties of surface oxygen vacancies in ZnO *interwoven* and *flower-like* nanosheets trusting that PL is a direct method to observe various behaviors of defects such as oxygen vacancies and zinc interstitials [17, 80].

The PL spectra of ZnO *interwoven* and *flower-like* nanosheets investigated at wavelength 340 nm excitation are shown in Fig. 10. Both PL spectra were fitted with a five Gaussian functions at the center wavelengths of 390 nm

(UV), 420 nm (violet), 466 nm (blue), 485 nm (blue–green), and 520 nm (green), which reproduces the PL spectrum more reasonably. The UV emission around 390 nm (3.17 eV) corresponds to near-band-edge (NBE) emission [81]. The band edge emission is mainly due to radiative recombination of excitons. The emission at 420 nm (2.95 eV) is attributed to the transition between shallow donors (oxygen vacancy) to the valence band VB [28–30]. The peak at 465 nm (2.66 eV) is related to zinc vacancy and interstitial defects [82]. The emission at 485 nm (2.55 eV) wavelength was assigned to recombination between the oxygen vacancy and interstitial oxygen, and lattice defects related to oxygen and zinc vacancies [83, 84]. A broad peak around 520 nm (2.38 eV) is due to radiative recombination of a photogenerated hole with an electron occupying the oxygen vacancy, which is attributed to the single ionized oxygen vacancy [85]. These transitions confirm the existence of the oxygen and zinc vacancies in both the *interwoven* and *flower-like* nanosheets. Therefore, the enhanced photocatalytic activity may be attributed to the presence of both UV and visible emission in both of the ZnO nanostructures as indicated in PL spectra.

The absorption of UV and visible spectrum from sunlight by ZnO nanosheets would excited to create electron–hole pairs [72], which react further according to the following reactions Eqs. (1)–(8):

$$ZnO + h\nu \rightarrow h^+ + e^- \tag{1}$$

$$h^+ + H_2O \rightarrow OH^{\cdot} + H^+ \tag{2}$$

$$h^+ + OH^- \rightarrow OH^{\cdot} \tag{3}$$

$$e^- + O_2 \rightarrow O_2^{\cdot -} \tag{4}$$

$$O_2^{\bullet -} + H_2O \rightarrow HO_2^{\cdot} + OH^{\cdot} \tag{5}$$

$$HO_2^{\cdot} + H_2O \rightarrow H_2O_2 + OH^{\cdot} \tag{6}$$

$$H_2O_2 \rightarrow 2OH^{\cdot} \tag{7}$$

$$\left. \begin{array}{l} MB + OH^{\cdot} \\ MB + O_2^{\cdot -} \end{array} \right\} \rightarrow \begin{array}{l} CO_2 + H_2O \\ + \text{Degraded products} \end{array} \tag{8}$$
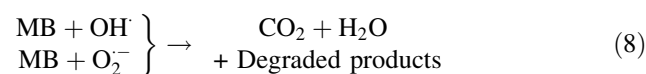
The schematic of photocatalytic mechanism, occurring in dye-photocatalyst solution under the sunlight irradiation, is shown in Fig. 11.

As compared with previous studies, a significant enhancement in photodegradation efficiencies, *interwoven* sheets 99.94 %, and *flower-like* nanosheets 79.76 %, while irradiated for 120 min, cannot be attributed only to the

Fig. 10 PL spectra of ZnO nanosheets, grown in **a** ethanol, and **b** water mediums, respectively. The *black solid curves* are the experimental data, and the *green curves* are individual peaks from the fittings. Spectra are recorded at 340 nm excitation wavelength
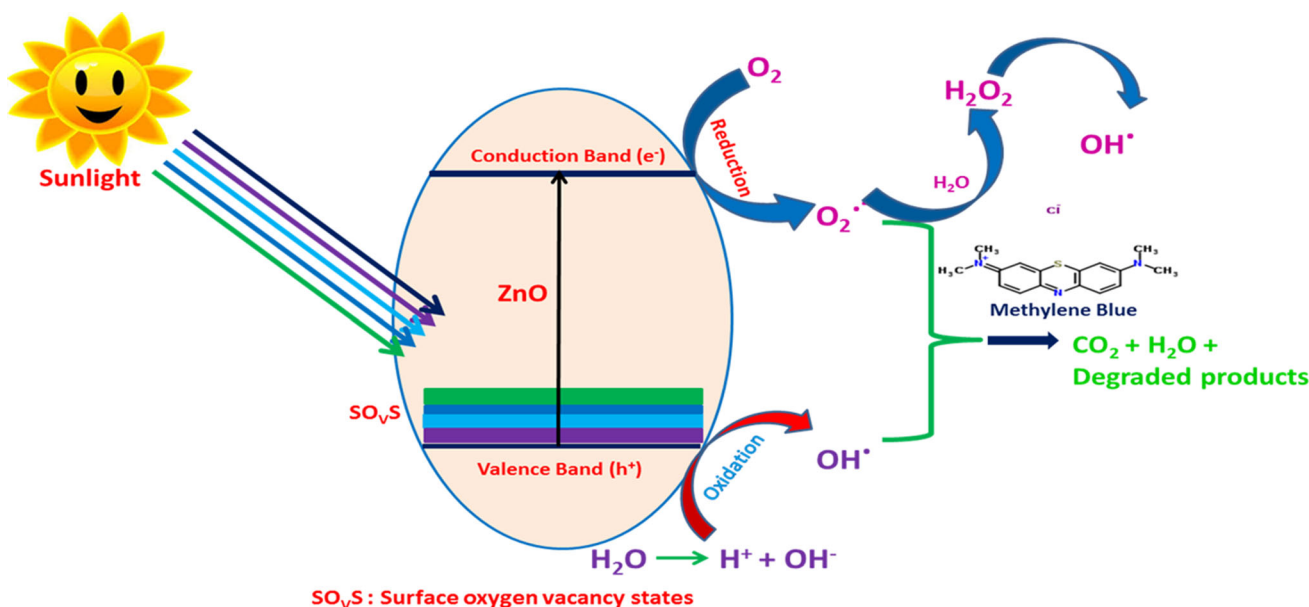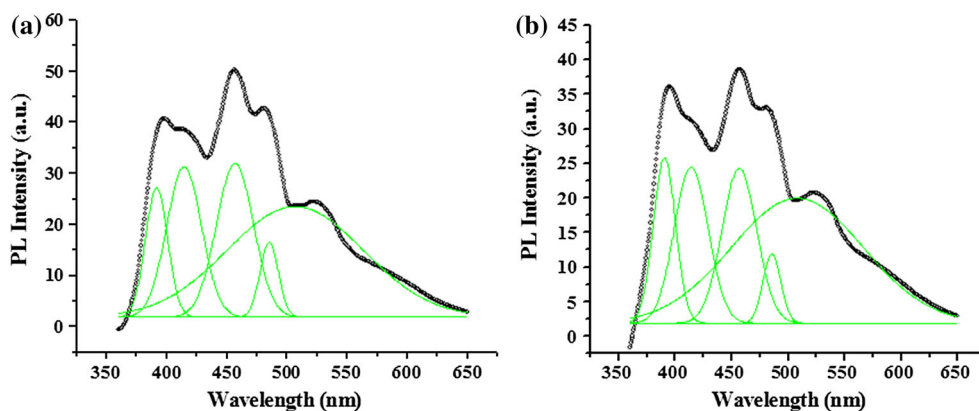
Fig. 11 Schematic representation of photocatalytic mechanism for the degradation of MB dyes in the presence of ZnO nanosheets under sunlight irradiation

surface oxygen vacancies but also the faceted geometry and large surface area of ZnO nanosheets. As observed from the SEM and TEM characterizations, the nanosheet structures have more surface defects generated. As reported earlier [86, 87], in our case too, the nanosheets with unique surface orientation exhibit high density of atomic steps and ledges, which serve as active sites for breaking chemical bonds, enhancing the photocatalytic activity. The observed difference between the degradation efficiencies of *interwoven* and *flower-like* nanosheets indicates that the morphology of ZnO influences the production of OH and O_2^-. So far the surface area effect is considered; the samples were characterized using BET measurement. Here, the *interwoven* nanosheets show higher surface area (11.765 m^2/g) as compared with *flower-like* nanosheets (10.247 m^2/g). The difference in the surface area of nanosheets would effect the production of free radicals responsible for photocatalytic activity. Further, in case of

flower-like structure, the nanosheets being in aggregated form perform less efficiently as compared to *interwoven* nanosheets. When *interwoven* nanosheets are used as photocatalyst in the solution, each of the nanosheet get dispersed availing its whole surfaces for photocatalytic reaction and, hence, a higher photocatalytic efficiency. The *flower-like* nanosheets due to aggregation tendencies do not completely expose their surface for sunlight irradiation, resulting in less production of OH· and O_2^- radicals. Conclusively, in our case, the photocatalytic activity is clearly dependent on the morphology, oxygen vacancies, and textures of ZnO nanostructures formed [87–89].

Conclusions

A facile, cost-effective, and room temperature solution route is developed to fabricate the large-scale surfactant free

interwoven and *flower-like* nanosheets of ZnO. The existence of hydrogen bonding among ZnO nanocrystals is less prominent when the C_2H_5OH medium is used due to the presence of ethyl group and, hence, lesser aggregation of ZnO nanocrystals, which results in the formation of *interwoven* nanosheets with the passage of reaction. The presence of surface oxygen vacancies, faceted structure, and large surface area resulted in enhanced photocatalytic efficiency of both ZnO nanostructures. The *flower-like* nanosheets due to aggregation tendencies do not completely expose their surfaces when irradiated in sunlight irradiation, resulting in less production of OH and O_2^- radicals and, hence, a lower degradation efficiency of MB dye.

References

1. Gonzalez-Valls I, Lira-Cantu M (2009) Vertically-aligned nanostructures of ZnO for excitonic solar cells: a review. Energy Environ Sci 2:19–34
2. Lai E, Kim W, Yang P (2008) Vertical nanowire array-based light emitting diode. Nano Res 1:123–128
3. Jin Y, Wang J, Sun B, Blakesley JC, Greenham NC (2008) Solution-processed ultraviolet photodetectors based on colloidal ZnO nanoparticles. Nano Lett 8(6):1649–1653
4. Zhang C, Zhang F, Xia T, Kumar N, Hahm JI, Liu J, Wang ZL, Xu J (2009) Low-threshold two-photon pumped ZnO nanowire lasers. Opt Express 17(10):7893–7900
5. Wei A, Wang Z, Pan LH, Li WW, Xiong L, Dong XC, Huang W (2011) Room-temperature NH_3 gas sensor based on hydrothermally grown ZnO nanorods. Chin Phys Lett 28:080702
6. Frenzel H, Lajn A, Wenckstern H, Lorenz M, Schein F, Zhang Z, Grundmann M (2010) Recent progress on Zno-based metal-semiconductor field-effect transistors and their application in transparent integrated circuits. Adv Mater 22:5332–5349
7. Hillman TR, Yamauchi T, Choi W, Dasari RR, Feld MS, Park Y, Yaqoob Z (2013) Digital optical phase conjugation for delivering two-dimensional images through turbid media. Sci Rep 3:1909
8. Choi Y, Yang TD, Fang-Yen C, Kang P, Lee KJ, Dasari RR, Feld MS, Choi W (2011) Overcoming the diffraction limit using multiple light scattering in a highly disordered medium. Phys Rev Lett 104:023902
9. Khokhra R, Kumar M, Rawat N, Barman PB, Jang H, Kumar R, Lee H (2013) Enhancing the numerical aperture of lenses using ZnO nanostructure-based turbid media. J Opt 15:125714
10. Garcia MA, Merino JM, Fernandez EP, Quesada A, Venta J (2007) Magnetic properties of ZnO nanoparticles. Nano Lett 7(6):1489–1494
11. Lim JH, Kang CK, Kim KK, Park IK, Hwang DK, Park SJ (2006) Electroluminescence emission from ZnO light-emitting diodes grown by high-temperature radiofrequency sputtering. Adv Mater 18:2720–2724
12. Lansdown ABG, Taylor A (1997) Zinc and titanium oxides: promising UV-absorbers but what influence do they have on the intact skin? Int J Cosmet Sci 19:167–172
13. Mohammad MT, Hashim AA, Al-Maamory MH (2006) Highly conductive and transparent ZnO thin films prepared by spray pyrolysis technique. Mater Chem Phys 99:382–387
14. Vempati S, Mitra J, Dawson P (2012) One-step synthesis of ZnO nanosheets: a blue-white fluorophore. Nanoscale Res Lett 7:470
15. Wang J, Liu P, Fu X, Li Z, Han W, Wang X (2009) Relationship between oxygen defects and the photocatalytic property of ZnO nanocrystals in Nafion membranes. Langmuir 25(2):1218–1223
16. Guo MY, Ng AMC, Liu FZ, Djurisic AB, Chan WK, Su HM, Wong KS (2011) Effect of native defects on photocatalytic properties of ZnO. J Phys Chem C 115:11095–11101
17. Li GR, Hu T, Pan GL, Yan TY, Gao XP, Zhu HY (2008) Morphology-function relationship of ZnO: polar planes, oxygen vacancies, and activity. J Phys Chem C 112:11859–11864
18. Becker J, Raghupathi KR, St. Pierre J, Zhao D, Koodali RT (2011) Tuning of the crystallite and particle sizes of ZnO nanocrystalline materials in solvothermal synthesis and their photocatalytic activity for dye degradation. J Phys Chem C 115:13844–13850
19. McLaren A, Valdes-Solis T, Li G, Tsang SC (2009) Shape and size effects of ZnO nanocrystals on photocatalytic activity. J Am Chem Soc 131(35):12540–12541
20. Jang ES, Won JH, Hwang SJ, Choy JH (2006) Fine tuning of the face orientation of ZnO crystals to optimize their photocatalytic activity. Adv Mater 18:3309–3312
21. Tian ZR, Voigt JA, Liu J, Mckenzie B, Mcdermott MJ, Rodriguez MA, Konishi H, Xu H (2003) Complex and oriented ZnO nanostructures. Nat Mater 2(12):821–826
22. Wang L, Chang LX, Zhao B, Yuan ZY, Shao GS, Zheng WJ (2008) Systematic investigation on morphologies, forming mechanism, photocatalytic and photoluminescent properties of ZnO nanostructures constructed in ionic liquids. Inorg Chem 47:1443–1452
23. Zhang L, Yang HQ, Ma JH, Li L, Wang XW, Zhang LH, Tian S, Wang XY (2010) Controllable synthesis and shape-dependent photocatalytic activity of ZnO nanorods with a cone and different aspect ratios and of short and fat ZnO microrods by varying the reaction temperature and time. Appl Phys A 100(4):1061–1067
24. Kong M, Li Y, Chen X, Tian T, Fang P, Zheng F, Zhao X (2011) Tuning the relative concentration ratio of bulk defects to surface defects in TiO2 nanocrystals leads to high photocatalytic efficiency. J Am Chem Soc 133(41):16414–16417
25. Justicia I, Ordejon P, Canto G, Mozos JL, Fraxedes J, Battiston GA, Gerbasi R, Figueras A (2002) Designed self-doped titanium oxide thin films for efficient visible-light photocatalysis. Adv Mater 14(19):1399–1402
26. Zuo F, Wang L, Wu T, Zhang ZY, Borchardt D, Feng PY (2010) Self-doped Ti^{3+} enhanced photocatalyst for hydrogen production under visible light. J Am Chem Soc 132(34):11856–11857
27. Wan Q, Wang TH, Zhao JC (2005) Enhanced photocatalytic activity of ZnO nanotetrapods. Appl Phys Lett 87(8):083105
28. Koch U, Fojtik A, Weller H, Henglein A (1985) Photochemistry of semiconductor colloids. Preparation of extremely small ZnO particles, fluorescence phenomena and size quantization effects. Chem Phys Lett 122(5):507–510
29. Hynek J, Kalousek V, Žouželka R, Bezdička P, Dzik P, Rathouský J, Demel J, Lang K (2014) High photocatalytic activity of transparent films composed of ZnO nanosheets. Langmuir 30(1):380–386
30. Bang S, Lee S, Ko Y, Park J, Shin S, Seo H, Jeon H (2012) Photocurrent detection of chemically tuned hierarchical ZnO nanostructures grown on seed layers formed by atomic layer deposition. Nanoscale Res Lett 7(1):290
31. Guo L, Ji YL, Xu H, Simon P, Wu Z (2002) Regularly shaped, single-crystalline ZnO nanorods with Wurtzite structure. J Am Chem Soc 124(50):14864–14865
32. Munoz-Espi R, Jeschke G, Lieberwirth I, Gomez CM, Wegner G (2007) ZnO-latex hybrids obtained by polymer-controlled crystallization: a spectroscopic investigation. J Phys Chem B 111(4):697–707

33. Pacholski C, Kornowski A, Weller H (2002) Self-assembly of ZnO: from nanodots to nanorods. Angew Chem Int Ed 41(7):1188–1191

34. Taubert A, Glasser G, Palms D (2002) Kinetics and particle formation mechanism of zinc oxide particles in polymer-controlled precipitation from aqueous solution. Langmuir 18(11):4488–4494

35. Tian ZR, Liu J, Voigt JA, Mckenzie B, Xu H (2003) Hierarchical and self-similar growth of self-assembled crystals. Angew Chem Int Ed 42(4):413–417

36. Umetsu M, Mizuta M, Tsumoto K, Ohara S, Takami S, Watanabe H, Kumagai I, Adschiri T (2005) Bioassisted room-temperature immobilization and mineralization of zinc oxide-the structural ordering of ZnO nanoparticles into a flower-type morphology. Adv Mater 17(21):2571–2575

37. Zhang T, Dong W, Keeter-Brewer M, Konar S, Njabon RN, Tian ZR (2006) Site-specific nucleation and growth kinetics in hierarchical nanosyntheses of branched ZnO crystallites. J Am Chem Soc 128(33):10960–10968

38. Zhang Y, Mu J (2007) Controllable synthesis of flower- and rod-like ZnO nanostructures by simply tuning the ratio of sodium hydroxide to zinc acetate. Nanotechnology 18(7):075606

39. Zou H, Luan Y, Ge J, Wang Y, Zhuang G, Li R, Li Z (2011) Synthesis of ZnO particles on zinc foil in ionic-liquid precursors. CrystEngComm 13(7):2656–2660

40. Zhang J, Wang J, Zhou S, Duan K, Feng B, Weng J, Tang H, Wu P (2010) Ionic liquid-controlled synthesis of ZnO microspheres. J Mater Chem 20:9798–9804

41. Kahn ML, Monge M, Colliere V, Senocq F, Maisonnat A, Chaudret B (2005) Size and shape control of crystalline zinc oxide nanoparticles: a new organometallic synthetic method. Adv Funct Mater 15(3):458–468

42. Monge M, Kahn ML, Maisonnat A, Chaudret B (2003) Room-temperature organometallic synthesis of soluble and crystalline ZnO nanoparticles of controlled size and shape. Angew Chem Int Ed 42(43):5321–5324

43. Antonietti M, Kuang D, Smarsly B, Zhou Y (2004) Ionic liquids for the convenient synthesis of functional nanoparticles and other inorganic nanostructures. Angew Chem Int Ed 43(38):4988–4992

44. Zhang J, Sun L, Yin J, Su H, Liao C, Yan C (2002) Control of ZnO morphology via a simple solution route. Chem Mater 14(10):4172–4177

45. Zhang X, Qin J, Xue Y, Yu P, Zhang B, Wang L, Liu R (2014) Effect of aspect ratio and surface defects on the photocatalytic activity of ZnO nanorods. Sci Rep 4:4596

46. Yang H, Cai W, Guo X (2014) Preparation and infrared emissivities of self-assembled ZnO spherical aggregates. Mater Sci Semicond Process 24:164–168

47. Liu D, Lv Y, Zhang M, Liu Y, Zhu Y, Zong R, Zhu Y (2014) Defect-related photoluminescence and photocatalytic properties of porous ZnO nanosheets. J Mater Chem A 2:15377–15388

48. Bai W, Zhu X, Zhu Z, Chu J (2008) Synthesis of zinc oxide nanosheet thin films and their improved field emission and photoluminescence properties by annealing processing. Appl Surf Sci 254(20):6483–6488

49. Cao B, Cai W, Li Y, Sun F, Zhang L (2005) Ultraviolet-light-emitting ZnO nanosheets prepared by a chemical bath deposition method. Nanotechnology 16(9):1734

50. Sun Y, Wang L, Yu X, Chen K (2012) Facile synthesis of flower-like 3D ZnO superstructures via solution route. CrystEngComm 14:3199–3204

51. Wang J, Hou S, Zhang L, Chen J, Xiang L (2014) Ultra-rapid formation of ZnO hierarchical structures from dilution-induced supersaturated solutions. CrystEngComm 16:7115–7123

52. Ma J, Su S, Fu W, Yang H, Zhou X, Huizhen Yao H, Chen Y, Yang L, Sun M, Mu Y, Lv P (2014) Synthesis of ZnO nanosheet array film with dominant 0001 facets and enhanced photoelectrochemical performance co-sensitized by CdS/CdSe. CrystEngComm 16:2910–2916

53. Xingfu Z, Zhaolin H, Yiqun F, Su C, Weiping D, Nanping X (2008) Microspheric organization of multilayered ZnO nanosheets with hierarchically porous structures. J Phys Chem C 112(31):11722–11728

54. Khoa NT, Kim SW, Thuan DV, Yoo DH, Kim EJ, Hahn SH (2014) Hydrothermally controlled ZnO nanosheet self-assembled hollow spheres/hierarchical aggregates and their photocatalytic activities. CrystEngComm 16:1344–1350

55. Banfield JF, Welch SA, Zhang H, Ebert TT, Penn RL (2000) Aggregation-based crystal growth and microstructure development in natural iron oxyhydroxide biomineralization products. Science 289(5480):751–754

56. Li P, Liu H, Zhang YF, Wei Y, Wang XK (2007) Synthesis of flower-like ZnO microstructures via a simple solution route. Mater Chem Phys 106(1):63–69

57. Jia B, Gao L (2008) Growth of well-defined cubic hematite single crystals: oriented aggregation and ostwald ripening. Cryst Growth Des 8(4):1372–1376

58. Vinogradov SN, Linnell RH (1971) Hydrogen bonding. Van Nostrand Reinhold Co, New York

59. Viswanatha R, Sarma DD (2007) Growth of nanocrystals in solution. In: Rao CNR, Müller A, Cheetham AK (eds) Nanomaterials chemistry: recent developments and new directions. Wiley-VCH Verlag GmbH & Co, KGaA, Weinheim, pp 140–157

60. Kawska A, Duchstein P, Hochrein O, Zahn D (2008) Atomistic mechanisms of ZnO aggregation from ethanolic solution: ion association, proton transfer, and self-organization. Nano Lett 8(8):2336–2340

61. Mo M, Yu JC, Zhang LZ, Li SKA (2005) Self-assembly of ZnO nanorods and nanosheets into hollow microhemispheres and microspheres. Adv Mater 17(6):756–760

62. Liu Y, Wang D, Peng Q, Chu D, Liu X, Li Y (2011) Directly assembling ligand-free ZnO nanocrystals into three-dimensional mesoporous structures by oriented attachment. Inorg Chem 50(12):5841–5847

63. Layek A, Mishra G, Sharma A, Spasova M, Dhar S, Chowdhury A, Bandyopadhyaya R (2012) A Generalized three-stage mechanism of ZnO nanoparticle formation in homogeneous liquid medium. J Phys Chem C 116(46):24757–24769

64. Li WJ, Shi EW, Zhong WZ, Yin ZW (1999) Growth mechanism and growth habit of oxide crystals. J Cryst Growth 203(1–2):186–196

65. Zhang DF, Sun LD, Yin JL, Yan CH, Wang RM (2005) Attachment-driven morphology evolvement of rectangular ZnO nanowires. J Phys Chem B 109(18):8786–8790

66. Xu S, Wang ZL (2011) One-dimensional ZnO nanostructures: solution growth and functional properties. Nano Res 4(11):1013–1098

67. Cheng B, Shi W, Russell-Tanner JM, Zhang L, Samulski ET (2006) Synthesis of variable aspect-ratio, single-crystalline ZnO nanostructures. Inorg Chem 45(3):1208–1214

68. Xu F, Shen Y, Sun L, Zeng H, Lu Y (2011) Enhanced photocatalytic activity of hierarchical ZnO nanoplate-nanowire architecture as environmentally safe and facilely recyclable photocatalyst. Nanoscale 3:5020–5025

69. Liao ZM, Lu Y, Wu HC, Bie YQ, Zhou YB, Yu DP (2011) Improved performance of ZnO nanowire field-effect transistors via focused ion beam treatment. Nanotechnology 22(37):375201

70. Zhang AQ, Zhang L, Sui L, Qian DJ, Chen M (2013) Morphology-controllable synthesis of ZnO nano/micro structures by a solvothermal process in ethanol solution. Cryst Res Technol 48(11):947–955

71. García-Rodríguez S (2013) Alternative metal oxide photocatalysts. In: Coronado JM, Fresno F, Hernández-Alonso MD, Portela

R (eds) Design of advanced photocatalytic materials for energy and environmental applications. Springer, London, p 106

72. Miao TT, Guo YR, Pan QJ (2013) The SL-assisted synthesis of hierarchical ZnO nanostructures and their enhanced photocatalytic activity. J Nanopart Res 15(6):1725

73. Eskizeybek V, Sarı F, Gulce H, Gulce A, Avc A (2012) Preparation of the new polyaniline/ZnO nanocomposite and its photocatalytic activity for degradation of methylene blue and malachite green dyes under UV and natural sun lights irradiations. Appl Catal B 119–120:197–206

74. Seema H, Kemp KC, Chandra V, Kim KS (2012) Graphene–SnO₂ composites for highly efficient photocatalytic degradation of methylene blue under sunlight. Nanotechnology 23(35):355705

75. Pons AJ, Sagués F, Bees MA, Sørensen PG (2000) Pattern formation in the methylene-blue–glucose system. J Phys Chem B 104(10):2251–2259

76. Dave MD, Pande UC (2013) Photoinduced electron transfer reaction of 2-thiobarbituric acid and methylene blue: mechanism and kinetics. Chem Sci Trans 2(3):749–760

77. Matsuoka M (1990) Other chromophores. In: Matsuoka M (ed) Infrared absorbing dyes. Plenum Press, New York, p 89

78. Salvador P, Garcia Gonzalez ML, Munoz F (1992) Catalytic role of lattice defects in the photoassisted oxidation of water at (001) n-titanium(IV) oxide rutile. J Phys Chem 96(25):10349–10353

79. Liu Y, Son WJ, Lu J, Huang B, Dai Y, Whangbo MH (2011) Composition dependence of the photocatalytic activities of BiOCl₁₋ₓBrₓ solid solutions under visible light. Chem Eur J 17(34):9342–9349

80. Warule SS, Chaudhari NS, Kale BB, More MA (2009) Novel sonochemical assisted hydrothermal approach towards the controllable synthesis of ZnO nanorods, nanocups and nanoneedles and their photocatalytic study. CrystEngComm 11:2776–2783

81. Yu W, Li X, Gao X (2005) Catalytic synthesis and structural characteristics of high-quality tetrapod-like ZnO nanocrystals by a modified vapor transport process. Cryst Growth Des 5(1):151–155

82. Liu B, Fu Z, Jia Y (2001) Green luminescent center in undoped zinc oxide films deposited on silicon substrates. Appl Phys Lett 79(7):943

83. Mahamuni S, Borgohain K, Bendre BS, Leppert VJ, Risbud SH (1999) Spectroscopic and structural characterization of electrochemically grown ZnO quantum dots. J Appl Phys 85(5):2861

84. Hu JQ, Ma XL, Xie ZY, Wong NB, Lee CS, Lee ST (2001) Characterization of zinc oxide crystal whiskers grown by thermal evaporation. Chem Phys Lett 344(1–2):97–100

85. Williams G, Kamat PV (2009) Graphene semiconductor nanocomposites: excited-state interactions between ZnO nanoparticles and graphene oxide. Langmuir 25(24):13869–13873

86. Lu Y, Wang L, Wang D, Xie T, Chen L, Lin Y (2011) A comparative study on plate-like and flower-like ZnO nanocrystals surface photovoltage property and photocatalytic activity. Mater Chem Phys 129(1–2):281–287

87. Umar A, Chauhan MS, Chauhan S, Kumar R, Kumar G, Al-Sayari SA, Hwang SW, Al-Hajry A (2011) Large-scale synthesis of ZnO balls made of fluffy thin nanosheets by simple solution process: structural, optical and photocatalytic properties. J Colloid Interface Sci 363(2):521–528

88. Tong Y, Cheng J, Liu Y, Siu GG (2009) Enhanced photocatalytic performance of ZnO hierarchical nanostructures synthesized via a two-temperature aqueous solution route. Scr Mater 60(12):1093–1096

89. Sun L, Shao R, Chen Z, Tang L, Dai Y, Ding J (2012) Alkali-dependent synthesis of flower-like ZnO structures with enhanced photocatalytic activity via a facile hydrothermal method. Appl Surf Sci 258(14):5455–5461